ADVANCED ENERGY MATERIALS
www.advenergymat.de

As-Doped Polycrystalline CdSeTe: Localized Defects, Carrier Mobility and Lifetimes, and Impact on High-Efficiency Solar Cells

*Patrik Ščajev, Marco Nardone, Carey Reich, Rouin Farshchi, Kevin McReynolds, Dmitry Krasikov, and Darius Kuciauskas**

The efficiency potential for single-junction photovoltaics (PV) is described by the detailed balance model, which requires the elimination of nonradiative recombination and perfect minority carrier collection. Improvements in GaAs, Si, and perovskite PV follow this model. It might be more complex for CdTe, a leading thin-film PV technology. While lifetime, passivation, and doping goals for 25% efficient CdTe solar cells are largely reached, voltage is ≈20% below the detailed balance limit. Why is that? In Se-alloyed $CdSe_xTe_{1-x}$ (Se is required for >20% efficiency) additional losses can occur due to electrostatic and bandgap fluctuations and due to electronic trap states. To understand mechanisms limiting CdSeTe solar cell performance and to suggest improvements, carrier dynamics, and transport in $CdSe_xTe_{1-x}$ with variation in Se composition and as doping is analyzed. It is shown that trapping, likely due to anion-site defects and their complexes, is correlated with low charge carrier mobility of 0.1–0.6 cm^2 $(Vs)^{-1}$. Even with 1000 ns charge carrier lifetimes, carrier diffusion length is less than the absorber thickness, reducing efficiency to ≈23%. Device simulations are used to analyze the performance of $CdSe_xTe_{1-x}$ solar cells; thermodynamic models are not sufficient for absorbers with electronic disorder and trapping.

1. Introduction

Alloying polycrystalline CdTe with Se enabled >20% efficient, manufacturable, large-scale (>16 GW will be installed in 2024) photovoltaics (PV). Efficiency and reliability were further augmented by transitioning from cation (Cd) site to anion (Se, Te) site doping,[1] which from 2024 is implemented in GW-scale manufacturing.[2] Current group-V doped CdSeTe solar cells have 23.1% certified efficiency and voltage from V_{OC} = 905 mV (record efficiency)[3] to 917 mV (record voltage),[4] while detailed balance voltage limit for E_g = 1.40 eV bandgap is 1122 mV.[5] Further progress in reducing voltage and fill factor (FF) losses and increasing cell efficiency is needed, as cell to module efficiency gap is decreasing.[6] CdTe PV research was focused on increasing minority carrier lifetime τ (controlling electron quasi-Fermi level) and doping p (controlling hole quasi-Fermi level) because modeling indicated that such improvements will lead to 25% efficient solar cells.[7] Metrics identified by modeling ($\tau \geq 100$ ns, surface recombination velocity SRV $\leq$ 100 cm s^{-1}, net doping $\geq 10^{16}$ cm^{-3}) were largely achieved due do group V doping[1] and mitigation of Shockley-Read-Hall (SRH) recombination in the absorber bulk (including grain boundaries)[8] and at polycrystalline

P. Ščajev
Institute of Photonics and Nanotechnology
Faculty of Physics
Vilnius University
Vilnius 10257, Lithuania

M. Nardone
Department of Physics
Bowling Green State University
Bowling Green, OH 43403, USA

The ORCID identification number(s) for the author(s) of this article can be found under https://doi.org/10.1002/aenm.202403902

DOI: 10.1002/aenm.202403902

C. Reich, R. Farshchi
California Technology Center
First Solar
Santa Clara, CA 95050, USA

K. McReynolds, D. Krasikov
Advanced Research
First Solar
Perrysburg, OH 43551, USA

D. Kuciauskas
Chemistry and Nanoscience Center
National Renewable Energy Laboratory
Golden, CO 80401, USA
E-mail: Darius.Kuciauskas@nrel.gov

interfaces.[9] CdSeTe absorbers are impacted by shallow semiconductor defects, which can reduce radiative voltage and trap charge carriers.[10] Shallow defects create band tails and localized defect states. Studies on absorbers fabricated using different processes (vapor transport deposition, close space sublimation, evaporation) identified radiative sub-bandgap defect states in CdSeTe.[10–14] Somewhat unexpectedly, we learned that near-E_g defects in CdSeTe are qualitatively different from CdTe.[10] In addition to quantifying thermodynamic voltage entitlement, understanding carrier dynamics is necessary for evaluating CdSeTe solar cells where trapping can have a large impact on performance. In this aspect, CdTe PV appears to differ from other mainstream PV technologies (GaAs, silicon, or perovskites), where external radiative efficiency data accurately predicts improvements.[15,16]

Solar cells and other electronic devices require efficient charge carrier collection when charge carrier diffusion length L_{diff} ($L_{diff} = \mathrm{sqrt}(\tau D)$, where diffusivity $D = kT/e\mu$; kT/e is thermal voltage, μ is mobility) several times exceeds absorber thickness.[17,18] While radiative and nonradiative recombination limits τ, defect scattering and trapping can limit μ. In CdTe, μ values can span a broad range. Time-resolved microphotoluminescence measurements find μ = 350–650 cm^2 (Vs)$^{-1}$ in undoped single crystal CdTe grown by molecular beam epitaxy (MBE),[19,20] light-induced transient grating (LITG) measurements find μ = 85–100 cm^2 (Vs)$^{-1}$ in undoped polycrystalline $CdSe_{0.2}Te_{0.8}$ films with large crystalline grains (L_{diff} approaching grain diameter).[21] Both intrinsic defects and impurities can limit mobility. Using Hall and photo-Hall measurements we reported (at 300 K) μ = 800 cm^2 (Vs)$^{-1}$ in Cl-compensated single crystal CdTe but μ = 10–100 cm^2 (Vs)$^{-1}$ in As-doped single crystals with low dopant activation.[22] Simulations for low-performance CdSeTe solar cells suggested that mobility decreases to μ < 0.1 cm^2 (Vs)$^{-1}$ is an important factor limiting performance, but the mechanisms of such mobility reduction were not identified.[23]

Here, we apply detailed measurements of electronic defects and carrier dynamics using a combination of spectrally- and time-resolved methods. We study polycrystalline CdSeTe heterostructures with uniform and graded bandgaps (graded bandgaps are used in record-efficiency solar cells)[24] and with different levels of As (group V dopant)[1] incorporation. Such correlative analysis of electronic defects and their impact is applied to polycrystalline PV absorbers for the first time: spectral photoluminescence (PL) quantifies near-E_g radiative defect states, time-resolved PL (TRPL) quantifies trapping, picosecond-resolution LITG quantifies initial mobility μ_1, nanosecond-resolution LITG quantifies mobility on the charge collection timescale μ_2, and pump-probe (PP) spectroscopy quantifies radiative and nonradiative state lifetimes. We show that initial mobilities in As-doped polycrystalline heterostructures (μ_1 = 5–60 cm^2 (Vs)$^{-1}$) are comparable with mobilities in single crystal CdTe:As with similar dopant activation (μ = 10–100 cm^2 (Vs)$^{-1}$).[22] Carrier trapping to the sub-E_g defect states (activation energies $E_{A,PL}$ = 60–165 meV) within less than 1 ns results in ≈50 times lower mobility, consistent with device simulations.[10,23] Trapping can impact carrier lifetimes – trapped carriers can be prevented from reaching SRH recombination centers, as was suggested for $ZnSe_xTe_{1-x}$.[25] In our samples and in highly-radiative passivated $CdSe_xTe_{1-x}$ absorbers[10,26] most radiative emission occurs from the trap states, therefore it is important to examine not only lifetime and radiative efficiency but also transport characteristics.

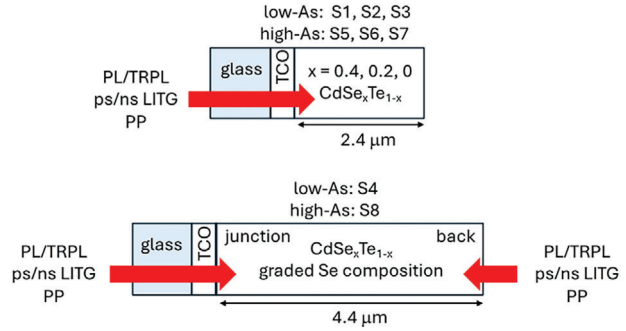

Scheme 1. $CdSe_xTe_{1-x}$ heterostructures S1–S8 and electro-optical measurements.

We show that sub-E_g defect states in $CdSe_xTe_{1-x}$ primarily introduce losses to devise performance by limiting charge carrier transport. This is a different loss mechanism than a reduction in radiative voltage due to sub-bandgap absorption and increased radiative recombination.[27–29] Impact on solar cells is quantified in device simulations, which agree with current CdTe PV efficiency records.

2. Samples and Methodology

We analyzed $CdSe_xTe_{1-x}$ heterostructures fabricated by vapor transport deposition (VTD) as a function of Se composition (x = 0, 0.2, and 0.4) and As incorporation (**Scheme 1** and **Table 1**). Heterostructures S1–S4 had background As (determined by secondary ion mass spectrometry, SIMS) while the other four samples had typical As density used in high-efficiency solar cells. The As dopant activation in doped heterostructures S5–S8 is 1–2%, which is state-of-the-art in polycrystalline absorbers.[4] Two heterostructures (S4,S8) had graded bandgap used in highly efficient CdSeTe solar cells.[1,4,24] The bandgap profile for graded samples is given in Ref. [30]; E_g increases from ≈1.4 eV near the front junction to ≈1.5 eV near the back contact.

Heterostructures S1–S8 did not have back contacts and optical measurements were applied from both sides. (LITG and PP are transmission-based measurements and require partially transparent samples at 1053 and 1064 nm probe wavelengths.) Sister samples were completed to devices using ZnTe back contacts[31] and capacitance-voltage (CV) was used to determine net p-doping. CV doping was p = (2-3) × 10^{15} cm^{-3} for S1,S3 and p = (1-2) × 10^{16} cm^{-3} for S6–S8. CV data was ambiguous for S1,S2, and S5.

3. Results and Discussion

3.1. Sub-Bandgap Defect States

Figure 1a–c shows glass-side PL emission spectra for $CdSe_{0.4}Te_{0.6}$ heterostructures S1 and S5. While bandgap at this composition is ≈1.38 eV,[32] most emission occurs at lower energies and is attributed to radiative defect states.[10–14] The level of As does not

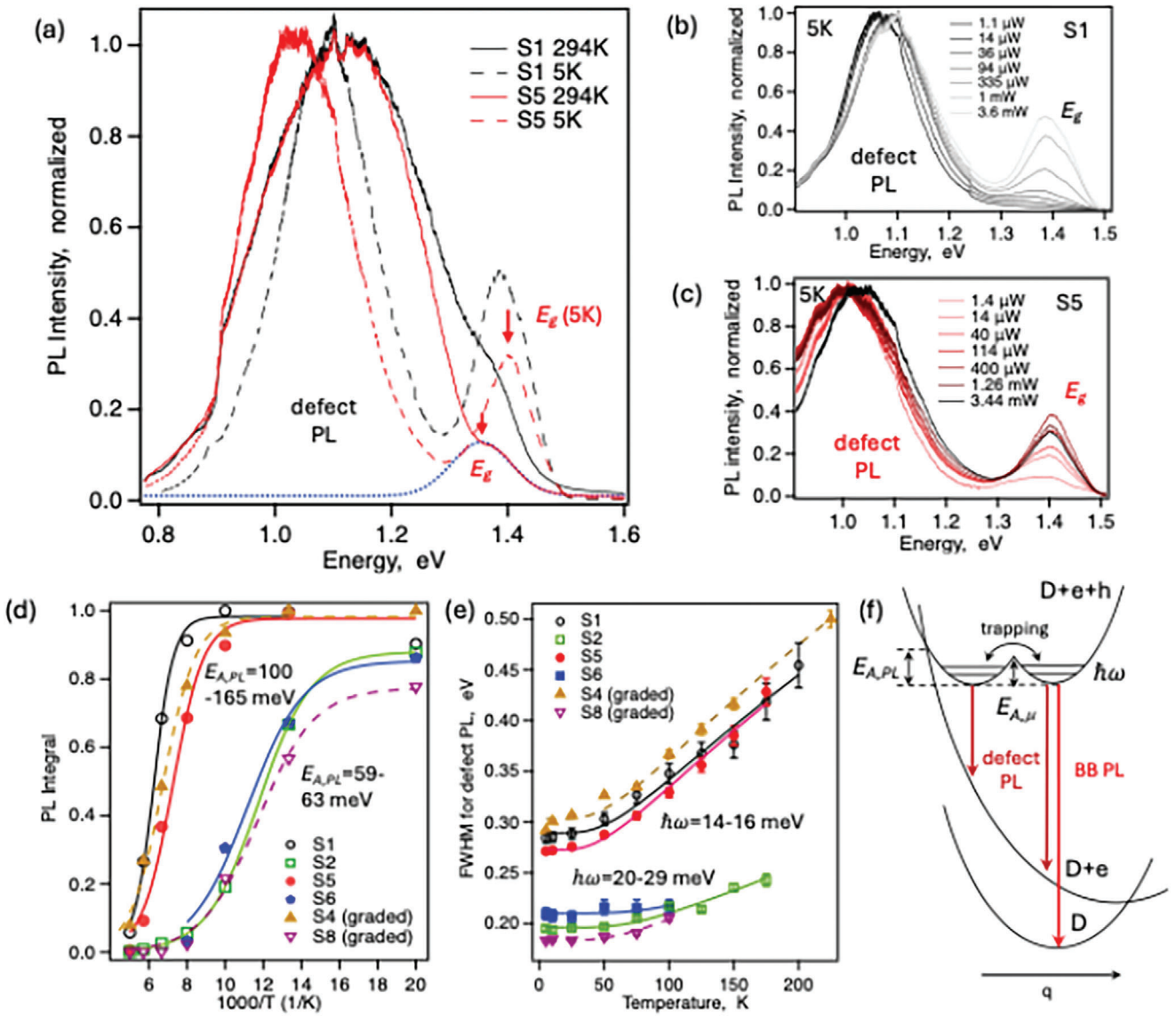

Figure 1. Analysis of radiative emission spectra. a) PL for heterostructures S1 and S5 at 294K (solid lines) and at 5 K (dashed lines). The Blue dotted line indicates bandgap emission (maximum at 1.354 eV) for S5 at 294 K. b,c) Injection-dependent PL spectra for S1 and S5 at 5 K. d) PL intensity temperature dependence for Se-containing heterostructures (data points) and fits to Equation (1) to determine $E_{A,PL}$. e) Analysis of spectral widths (FWHM) for defect emission. Solid lines are fit to Equation (2). f) Configuration coordinate diagram describing band-to-band (BB) and defect PL emission. D is the ground state, D+e+h is excited state where an electron has been excited from the valence band to the conduction band, D+e is excited state where the hole was captured by the defect. The configuration coordinate is q.

change radiative emission spectra substantially, which suggests that defect emission peak is not due to As dopants, but due to intrinsic and/or impurity defects. The absolute quantum yield of external radiative emission (PLQY) was determined at 294 K using 1-Sun equivalent photon fluence (2×10^{21} photons/(m^2s)) for this bandgap). PLQY increases about two times with higher As (Table 1).

$CdSe_{0.4}Te_{0.6}$ bandgap emission is observed as a shoulder at 294 K (blue dotted line in Figure 1a) and as a distinct peak at 5 K shifted by +45 meV, which is a typical bandgap increase for II–VI semiconductors of this bandgap at low temperature.[33] Injection-dependent PL emission spectra at 5 K (Figure 1b,c) more clearly resolve bandgap and defect emission bands. Only a limited spectral narrowing of the defect band at low temperatures (full width at half maximum FWHM = 616/555 meV at 294 K and 237/349 meV at 5 K for S1/S5) indicates a complex configurational diagram of the radiative defect state, which is analyzed next.

PL emission spectra for other heterostructures are given in Figures S1–S3 (Supporting Information). Broad defect emission dominates for $CdSe_{0.2}Te_{0.8}$ (S2,S6) and for graded $CdSe_xTe_{1-x}$ (S4,S8) compositions, but not for CdTe (S3,S7). This is in agreement with radiative emission assignments to Se-related defects.[10–14]

Table 1. Electrooptical characteristics of heterostructures S1–S8.

	$CdSe_xTe_{1-x}$	PLQY	$E_{A,PL}$, meV	S	$\hbar\omega$, meV	μ_1, cm^2 $(Vs)^{-1}$	μ_2, cm^2 $(Vs)^{-1}$	$E_{A,\mu}$, meV	τ_{LITG}, ns	τ_{TRPL}, ns	τ_{PP}, ns	L_{diff}, μm
low As	S1 (x = 0.4)	6.7×10^{-5}	165 ± 16	14.9 ± 0.2	15.9 ± 0.8	11/10	0.56/0.33	79 ± 13	742	508	820	0.9/0.8/1.0
	S2 (x = 0.2)	4.1×10^{-6}	63 ± 8	3.1 ± 0.1	23.6 ± 1.1	25/23	0.36/0.47	106 ± 6	394	36	105	0.7/0.2/0.3
	S3 (x = 0)	2.6×10^{-6}				37/42	0.5/0.25	123 ± 15	50	5.3	12	0.2/0.1/0.1
	S4 (graded x)	3.6×10^{-5}	100 ± 10	17.7 ± 0.2	15.3 ± 0.6	16/71	0.54/0.94	88/112	579	470	950	1.1/1.0/1.4
high As	S5 (x = 0.4)	1.4×10^{-4}	107 ± 16	16.6 ± 0.2	14.2 ± 0.5	4.6/7.1	0.16/0.23	88 ± 1	214	1084	850	0.3/0.7/0.7
	S6 (x = 0.2)	6.7×10^{-6}	59 ± 17	2.3 ± 0.1	29.4 ± 4.9	6.8/7.1	0.32/0.22	85 ± 8	390	132	430	0.5/0.3/0.5
	S7 (x = 0)	2.0×10^{-6}				62/-	0.87/0.37	111	61	4.1	3/95	0.3/0.1/0.1
	S8 (graded x)	1.3×10^{-4}	59 ± 6	3.9±0.1	19.7 ± 0.7	7.5/58	0.54/0.49	68/124	138	224	180	0.4/0.5/0.5

PLQY, PL emission quantum yield, $E_{A,PL}$, PL activation energy, S, Huang-Rhys factor, $\hbar\omega$, local vibrational energy, μ_1, μ_2, ambipolar charge carrier mobilities from ps- and ns-resolution LITG measurements. Two mobility values are given for each sample. The first was measured from the junction side and the second from the back side of the heterostructure, $E_{A,\mu}$ – mobility activation energy, τ_{LITG}, τ_{TRPL}, τ_{PP} – lifetimes measured with LITG, TRPL, and PP spectroscopies, L_{diff} is charge carrier diffusion length, $L_{diff} = \sqrt{\mu_2 \frac{kT}{e} \tau}$, estimated for τ_{LITG}, τ_{TRPL}, and τ_{PP}.

To determine defect activation energy $E_{A,PL}$, Huang – Rhys factor S, and local vibrational energy $\hbar\omega$, we analyzed the temperature dependence of PL emission (Figures S4 and S5, Supporting Information). Figure 1d shows integrated intensity and Figure 1e shows the spectral width (FWHM) of the defect emission for Se-containing heterostructures. Integrated intensity $PL(T)$ was fit to[33]

$$PL(T) = \frac{A}{1 + B exp\left(-\frac{E_{A,PL}}{kT}\right)} \quad (1)$$

where A and B are constants, k is Boltzmann's constant, and T is temperature. More detailed models can be applied to understand the temperature dependence of multiphonon processes.[34] The FWHM(T) for the defect band were fit to[33]

$$FWHM(T) = 2.36\sqrt{S}\hbar\omega\sqrt{coth\left(\frac{\hbar\omega}{2kT}\right)} \quad (2)$$

Fitting results are given in Figure 1d,e as solid lines and parameters $E_{A,PL}$, S, and $\hbar\omega$ are summarized in Table 1. Two groups of heterostructures are identified from this analysis. Lower Se (x = 0.2) heterostructures and graded heterostructure S8 have $E_{A,PL}$ = 59–63 meV, S = 2.3–3.9 eV, and $\hbar\omega$ = 20–29 meV. For these samples local vibrational energies are similar to LO phonon energies in single crystals, $\hbar\omega$ = 22.1 meV in CdTe and 26 meV in CdSe.[35] Higher-Se heterostructures (x = 0.4) and graded heterostructure S4 have higher activation energies $E_{A,PL}$ = 100–165 meV, larger S = 14.9–17.7, and more distorted local phonon energies $\hbar\omega$ = 14–16 meV. The differentiation of defect properties into two groups dependent on Se composition suggests that radiative centers are not simple point defects but larger complexes, and their density likely increases with Se.

While emission occurs well below the bandgap (down to 0.8 eV, Figure 1; Figures S1 and S3, Supporting Information) $E_{A,PL}$ are relatively small and defects are relatively shallow. Similar characteristics are common for defects with large structural relaxation in the excited state, for example, anion V_{Se} vacancies in $CuInSe_2$ and $CuGaSe_2$.[36] Anion-site substitution in II–VI semiconductors can lead to carrier localization and trapping, which can be examined with emission spectroscopy.[37] For example, in $ZnSe_xTe_{1-x}$ radiative defects were attributed to lattice distortions at tellurium sites due to coupling of the p-orbitals at the valence band maximum.[25] In CdS_xSe_{1-x}, emission was attributed to localized exciton band.[38] In CdSe, localized radiative centers were attributed to V_{Se} and O_{Se} point defects.[35] First-principles analysis in $CdSe_{0.96}Te_{0.04}$ attributed defects to V_{Se} interacting with Te sites.[39] These characteristics can be modified by doping. Especially when dopant incorporation is high (≈10^{18} cm^{-3} for As doping in $CdSe_xTe_{1-x}$) and activation is low (1–2% is typical), compensation can create electrostatic potential fluctuations. Data in Figure 1; Figures S1 and S3 (Supporting Information) does not indicate electrostatic potential fluctuations as analyzed by Moseley et al. in As-doped CdTe.[40] Therefore, in CdSeTe absorbers, intrinsic defects (and/or common impurities, such as O and Cl) more strongly impact electronic properties than compensation due to incomplete dopant activation.[10]

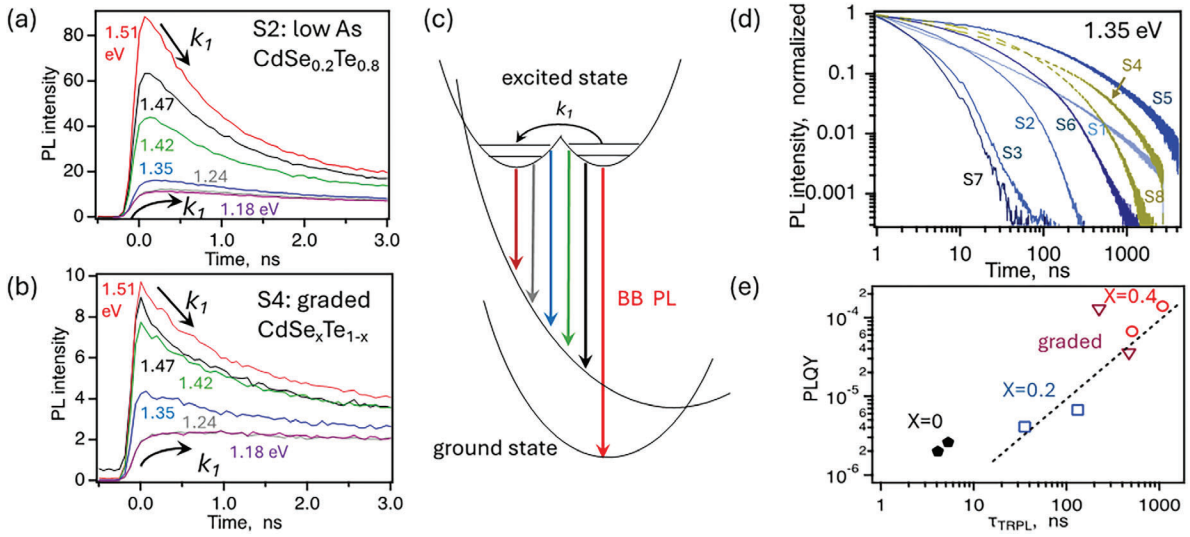

Figure 2. a,b) TRPL decays at emission energies indicated in the legends for heterostructures S2 and S4. c) Configuration coordinate diagram indicating excited state energy barrier (barrier crossing rate k_1) and emission energies for band to band (BB) and defect PL. d) Full TRPL decays (at 1.35 eV) for heterostructures S1–S8. e) Comparison of PL emission quantum yield (PLQY) and TRPL lifetimes. The dashed line is a guide to the eye showing linear PLQY increase with τ_{TRPL}.

The configuration diagram in Figure 1f geometrically indicates $E_{A,PL}$ and $\hbar\omega$ parameters and band-to-band (BB) and defect radiative emission. By using this diagram, we consider excited state carrier dynamics including defect scattering (barriers $E_{A,\mu}$) and trapping.[10,23,25]

3.2. Carrier Trapping Dynamics

Because defects dominating radiative emission are localized centers (not delocalized band tail states[40]) they can trap photogenerated carriers and reduce charge carrier diffusion length.[10] Trapping signatures are directly shown using TRPL, **Figure 2**, where graphs (a) and (b) display kinetics at emission energies from 1.51 to 1.18 eV for heterostructures S2 and S4. Corresponding TRPL data for other heterostructures is given in Figure S6 (Supporting Information).

Rate constant k_1 indicates fast (k_1^{-1} = 0.3 ns) decay of the bandgap emission (at 1.51, 1.47, and 1.42 eV) and increase of defect PL intensity with the same rate (at 1.24 and 1.18 eV). Rate constant k_1 is attributed to crossing excited state barriers (Figure 2c). Because the excited state barrier is relatively small (see next Section for barrier measurement using LITG), carriers can equilibrate between the minima in the excited state. As a result of such trapping/detrapping, starting from ≈3 ns lifetimes are the same at all emission energies. Longer-time TRPL decays for all heterostructures are given in Figure 2d. Single-exponential fits were used to determine the lifetimes τ_{TRPL} from wavelength-independent TRPL decays, Table 1. Lifetimes range from τ_{TRPL} = 4.1–5.3 ns (S3 and S7, typical values for CdTe without Se alloying[41]) to τ_{TRPL} = 508–1084 ns (S1 and S5). A similar lifetime dependence on composition x was reported.[8] Detailed TRPL lifetime modeling in samples with the junction field was reported in Refs. [30,42]

Figure 2e shows that PLQY increases with τ_{TRPL}. For heterostructures with x = 0.2 and x = 0.4, PLQY increase is approximately linear (dashed line). Graded heterostructures with intermediate Se composition have τ_{TRPL} and PLQY in the intermediate range. Graded and x = 0.4 heterostructures have lifetimes sufficient for 25% efficient solar cells.[7] However, the excited state energy surface is more complex with barriers between the energy minima (Figure 2c), and charge carrier mobilities are reduced by defect scattering and trapping, shortening L_{diff}. Next, we analyze these effects.

3.3. Free and Trapped Carrier Diffusivity (Mobility)

We used light-induced transient grating (LITG) spectroscopy to directly measure lateral charge carrier diffusivity over the distance of 1–3 μm (grating period Λ). To analyze carrier transport before and after trapping, LITG measurements were performed using the same excitation (10 ps pulses at 527 nm) but probing carrier diffusion and recombination on picosecond (ps) and nanosecond (ns) time scales, as explained below.

For LITG spectroscopy two excitation beams, intersecting at an angle Θ, create an interference pattern with a period $\Lambda \approx \lambda_{527nm}/\sin(\Theta)$ in the sample (**Figure 3a**). The light-induced spatial modulation of carrier density $\Delta N \propto (1+\cos(\frac{2\pi x}{\Lambda}))$ was monitored by the diffraction of probe beams at 1053 nm (10 ps pulses, fast grating, Figure 3b) and 1064 nm (2 ns pulses, slow grating, Figure 3c). LITG data for other heterostructures are given in Figures S7 and S8 (Supporting Information).

The gratings decay exponentially (grating lifetime τ_G) due to carrier diffusion (diffusion lifetime τ_D) and recombination (recombination lifetime τ_{LITG}). We varied grating periods Λ using

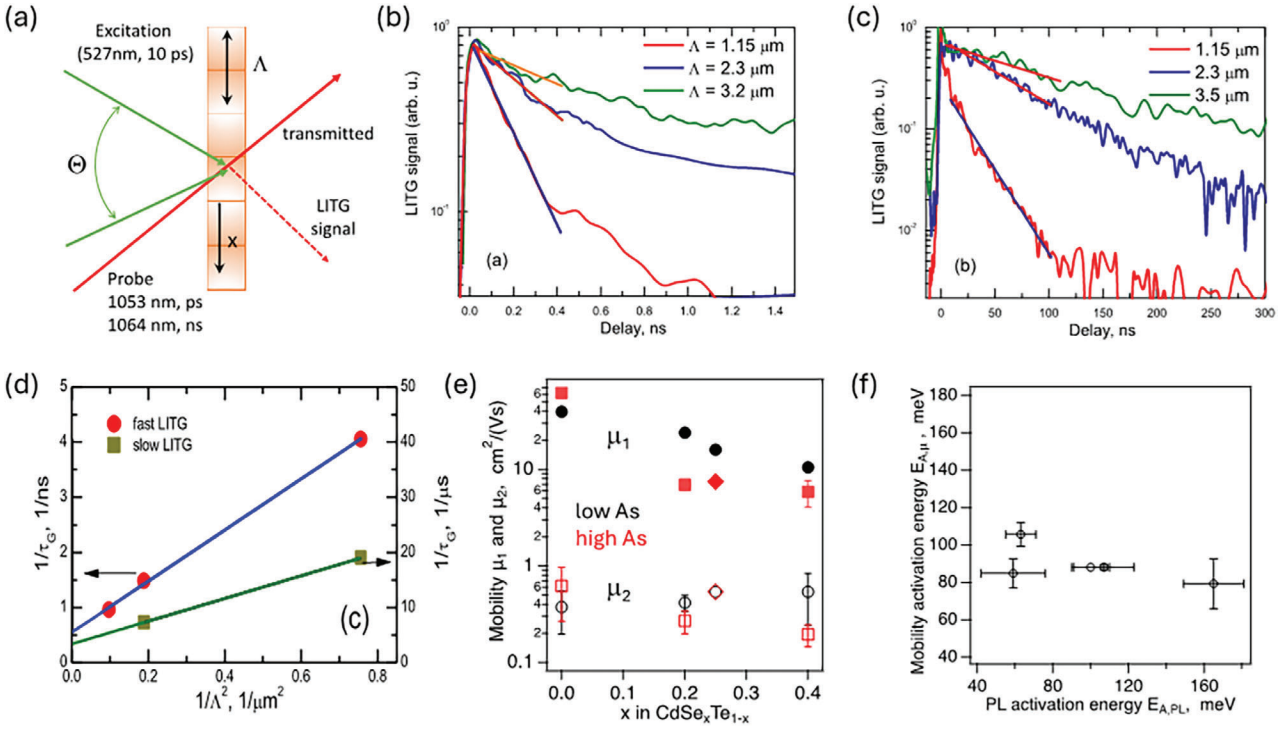

Figure 3. Light-induced transient grating (LITG) data and analysis. a) Illustration of LITG measurement. The grating period Λ is set by the angle (Θ) between two excitation beams and excitation wavelength (527 nm). Part of the probe beam is diffracted from the grating (LITG signal). The time dependence of LITG signal indicates carrier diffusion and recombination. b) "Fast" and c) "slow" LITG data for $CdSe_{0.2}Te_{0.8}$:As heterostructure S6 and grating periods Λ indicated in legends. Single exponential fits (shown as solid lines) indicate grating decay times τ_G for each geometry and time resolution. d) Analysis of $1/\tau_G$ versus $1/\Lambda^2$ data to determine diffusivity (proportional to the slope of the linear fit) and recombination lifetime τ_{LITG} (inverse intercept of y-axis). e) Mobilities μ_1 and μ_2 for all heterostructures (Table 1). f) Correlation of mobility and PL activation energies.

three angles Θ, and calculated diffusion and recombination components using[43]

$$\frac{1}{\tau_G} = \frac{1}{\tau_{LITG}} + \frac{1}{\tau_D} = \frac{1}{\tau_{LITG}} + \frac{4\pi^2 D}{\Lambda^2} \tag{3}$$

where recombination rate $(1/\tau_{LITG})$ and diffusion rate $(1/\tau_D)$ are additive. Grating lifetimes τ_G are analyzed versus grating period Λ in Figure 3d, where solid lines indicate fits to Equation (3). Slopes of linear fits indicate $D_1 = 0.18$ cm^2/s and $D_2 = 8.3 \times 10^{-3}$ cm^2 s^{-1}, corresponding to mobilities $\mu_1 = 6.8$ cm^2 (Vs)$^{-1}$ and $\mu_2 = 0.32$ cm^2 (Vs)$^{-1}$ for heterostructure S6.

Data measured through glass substrates can be impacted by the junction field, and data measured from the back side can be impacted by the surface recombination. To evaluate the impact of these effects, we performed LITG measurements from both sides. For nongraded heterostructures, mobilities for junction and back sides are similar (both values are given in Table 1), indicating that LITG data mostly reflects bulk diffusion and recombination, not interface or drift effects. Because of relatively high injection (see next Section where injection dependence is reported), diffusivities and mobilities in this study are ambipolar, D_a and μ_a. They are related to electron and hole properties as $\mu_a = \frac{2\mu_e\mu_h}{\mu_e+\mu_h}$. Because hole effective mass is ≈4 times higher in CdTe, $\mu_a \approx 2\mu_h$.

For all samples, we find that ns-scale mobility μ_2 is ≈50 times lower than the initial mobility μ_1.[44] This reduction in mobility in less than 1 ns is attributed to trapping. Using the model from disordered semiconductors we can quantify the difference between μ_1 and μ_2 using mobility activation energy $E_{A,\mu}$

$$E_{A,\mu} = kT\ln\left(\frac{\mu_1}{\mu_2}\right) \tag{4}$$

Parameters of LITG analysis (μ_1, μ_2, and $E_{A,\mu}$) are given in Table 1; uncertainty in $E_{A,\mu}$ is calculated by averaging junction and back-side mobilities. Figure 3e graphically summarizes mobility data. Several aspects are interesting and important for thin film solar cells.

First, μ_1 and μ_2 do not significantly depend on the doping level. (Similar trends were observed with PL and TRPL, Sections 3.1 and 3.2.) This supports the earlier suggestion that electronic defects (in this case, scattering centers) are primarily due to Se alloying, but not due to low As-dopant activation and resulting compensation.[40]

Second, initial mobilities μ_1 are relatively high and similar to values used in device simulations. For example, Ref. [7] used $\mu_e = 320$ cm^2/(vs) and $\mu_h = 80$ cm^2/(vs), implying $\mu_a = 128$ cm^2/(vs). Nardone et al used $\mu_e = 100$ cm^2/(vs),[45] implying $\mu_a = 40$ cm^2/(vs). We reported LITG mobilities $\mu_1 = 85$–100 cm^2 (Vs)$^{-1}$ (measured with ps resolution) for Al_2O_3-passivated $CdSe_{0.2}Te_{0.8}$ double heterostructures fabricated by

evaporation and annealed at high temperature to increase crystalline grain sizes up to 10 μm.[21] Interface passivation with Al_2O_3 increased PLQY and τ_{TRPL} by more than an order of magnitude,[21] but initial mobilities for our VTD-fabricated samples with smaller grains are only somewhat lower; $\mu_1 \approx$ 23–25 cm^2 $(Vs)^{-1}$ for $CdSe_{0.2}Te_{0.8}$ heterostructure S2.

Third, μ_1 decreases with x from 40–60 $cm^2/(Vs)$ for S3/S7 (x = 0) to 7 – 10 $cm^2/(Vs)$ for S1/S5 (x = 0.4). In contrast, μ_2 is approximately constant at 0.2–0.6 $cm^2/(Vs)$ for all x compositions, indicating that disordered transport on ns time scale does not substantially change with Se composition.

Fourth, initial mobility μ_1 is more complex in graded samples. It is higher from the back (x ≈ 0) than for the CdSeTe region near the front junction (x ≈ 0.25), confirming a gradual μ_1 decrease with x. PL analysis also indicated defect dependence on x ($E_{A,PL}$ in Table 1). We examine if PL defects and mobility-limiting defects are correlated by plotting $E_{A,PL}$ versus $E_{A,\mu}$ in Figure 3f. Because correlation is absent, it appears that PL-defects and scattering centers have different origins, which is reflected in the configuration diagram in Figure 1f.

Fifth, ns-scale mobility is lower in all samples, which is unexpected. PL/TRPL and earlier work[10–14] indicated that only CdSeTe alloys have strong sub-bandgap radiative emission. CdTe absorbers have PL bands attributed to dopants and other defects,[46,47] but CdTe absorbers without Se do not have substantial losses in radiative voltage and do not exhibit carrier trapping.[10] One possibility is that As-doping introduces electrostatic potential fluctuations in S3 and S7, as reported by Moseley et al for As-doped CdTe.[40] This aspect needs to be investigated in the future, as the origin and impact of electrostatic potential fluctuations in doped CdTe differs from localized anion-site defects in CdSeTe analyzed here.

3.4. Carrier lifetime analysis

Minority carrier lifetime τ is a key characteristic in solar cells (it determines minority carrier quasi-Fermi level) and in Cd(Se)Te solar cells τ is usually measured using TRPL.[41,68] While detailed modeling is needed to interpret TRPL data in devices,[30] using other measurements (such as transient photovoltage) yields similar lifetimes when both techniques can be applied.[48] When carrier dynamics is more complex, such as with excited state trapping, radiative and nonradiative states can have different lifetimes. For example, in As-doped single crystal CdTe, TRPL lifetimes were limited by surface recombination, while nonradiative bulk lifetimes were up to 35 μs.[22] Here, we report and compare lifetimes measured with TRPL (Figure 2d, τ_{TRPL} in Table 1), LITG (Figure 3, τ_{LITG} in Table 1), and pump-probe (PP) spectroscopy.

PP kinetics for heterostructure S6 are shown in **Figure 4a**. At high excitation fluence (71 μJ cm^{-2}) PP decays are dominated by radiative recombination, while at the lowest fluence (2.1 μJ cm^{-2}) a single-exponential decay (fit is shown with a solid line) indicates SRH recombination and PP lifetime is τ_{PP} = 430 ns. PP kinetics for other heterostructures are shown in Figure S9 (Supporting Information).

Single-exponential fits for the lowest injection data were used to determine τ_{PP} in Table 1. PP and LITG measurements were performed for a range of excitation densities; injection-dependent lifetimes are summarized in Figure 4b and injection-dependent ambipolar diffusivities in Figure 4c. To calculate injection from the excitation fluence, we assumed 0.1 μm absorption depth. When carriers equilibrate over the 2.4 μm thick absorber (Scheme 1), injection is ≈24 times lower, ≥5 × 10^{15} cm^{-3} for PP spectroscopy, less than $p \approx 10^{16}$ cm^{-3} in doped heterostructures. Injection lower than doping allows SRH lifetime determination directly from fit lifetimes. The transition from radiative to SRH recombination when decreasing excitation fluence is evident in Figure 4b, where τ_{PP} asymptotically approaches injection-independent values at the lowest fluence.[49]

Diffusivities D_a (Figure 4c) also approach asymptotic values, and the lowest values are reported in Table 1 ($D_a = \frac{kT}{e}\mu_2$). At higher fluence, photogenerated carriers screen scattering centers and mobilities/diffusivities increase. The D_a increase by about an order of magnitude for low-As heterostructures S1–S4 suggests that more than one type of scattering center is present and that the density of scattering centers is <10^{18} cm^{-3}.[43] For doped heterostructures S5–S8 D_a increase with injection is ≈2 times smaller, presumably because >10^{18} cm^{-3} As-related scattering centers are dominant in doped samples.

Lifetimes τ_{LITG}, τ_{TRPL}, and τ_{PP} are compared in Figure 4d. Comparison also includes PLQY, which is measured at 1-Sun equivalent photon fluence and according to thermodynamic models indicates recombination losses in solar cells.[17] Four metrics (τ_{LITG}, τ_{TRPL}, τ_{PP}, and PLQY) are in approximate but not exact agreement.

Lifetime τ_{LITG} differs the most from the other three characteristics, especially for x = 0 heterostructures S3 and S7. This is likely because LITG measurement requires higher injection (modulated photocarrier density needs to allow measurable diffraction of the probe beam, Figure 3a). In addition, x = 0 heterostructures have high mobilities μ_1, and data can be impacted by the lateral carrier redistribution which changes the relative contributions of radiative versus nonradiative recombination. For CdSeTe heterostructures (x≠0) transport is slower and τ_{LITG} are similar to τ_{PP}.

Lifetime τ_{TRPL} correlates with PLQY best, within 2× or less using ranges chosen in Figure 4d (larger difference for x = 0.2 heterostructures S2 and S6 with shallower PL defects). Good τ_{TRPL} and PLQY correlation was also shown in Figure 2e and in Onno et al.[26] While PL uses continuous and TRPL uses pulsed excitation, both experiments are more sensitive (than PP and LITG) to surface effects,[22,43] and surface/interface recombination is large in Cd(Se)Te solar cells.[31]

Agreement between τ_{LITG}, τ_{PP}, τ_{TRPL}, and PLQY indicates that minority carrier lifetimes are determined accurately, in part because carrier traps and scattering centers are relatively shallow, $E_{A,PL}$ = 69–165 meV and $E_{A,\mu}$ = 68–124 meV. Only when $E_{A,PL}$ ≥200 meV trapping is largely irreversible at 294 K.[10]

We use lifetime and mobility data to estimate charge carrier diffusion length $L_{diff} = \sqrt{\mu_2 \frac{kT}{e} \tau}$, where $\tau = \tau_{LITG}$, τ_{TRPL}, and τ_{PP}. Diffusion lengths range from L_{diff} = 0.1–0.3 μm for CdTe to L_{diff} = 0.8–1.4 μm for $CdSe_{0.4}Te_{0.6}$ (Table 1). These relatively low L_{diff} values illustrate the impact of reduced mobility μ_2-even with

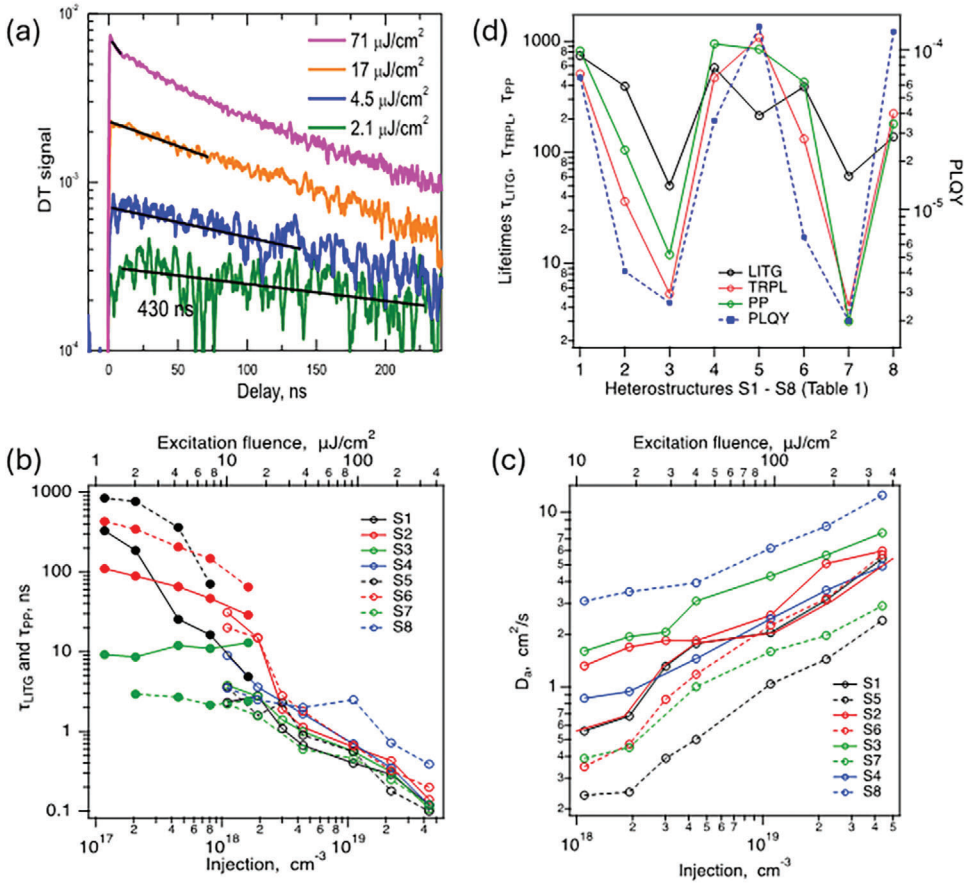

Figure 4. Carrier lifetime analysis. a) PP decays for $CdSe_{0.2}Te_{0.8}$:As heterostructure S6 with excitation fluences indicated in the legend. Solid lines show single exponential fits indicating τ_{PP} lifetimes. b) Lifetimes τ_{LITG} (open circles) and τ_{PP} (filled circles) versus injection and excitation fluence. Solid lines show data for high-As heterostructures S5–S8, dashed lines show data for low-As heterostructures S1–S4. c) Diffusivities D_a corresponding to τ_{LITG} in (b). d) Comparison of τ_{LITG}, τ_{PP},τ_{TRPL}, and PLQY. PP and TRPL lifetimes were measured at 2 μJ cm^{-2}, LITG lifetimes were measured at 10 μJ cm^{-2}, and PLQY were measured at 1 Sun equivalent excitation. Data in (d) is also given in Table 1.

lifetimes ranging from $\tau_{TRPL} = 508$ ns to $\tau_{pp} = 820$ ns (S1), diffusion length is shorter than the absorber thickness. The radiative lifetime $\tau_R = (B\,p)^{-1} \approx 1$ μs (if $p \approx 10^{16}$ cm^{-3} and radiative recombination coefficient $B \approx 10^{-10}$ cm^3 s^{-1}[50]). For L_{diff} to exceed absorber thickness when μ_2 has values reported in this study, carrier density must be $<10^{16}$ cm^{-3}. Such low-doping cases could potentially enable high L_{diff}, with corresponding requirements for bulk and interface passivation.

3.5. Impact on CdSeTe Solar Cells

We estimate the effect of reduced mobilities on the performance of a solar cell with a graded CdSeTe absorber, where the graded Se profile allows for higher current (J_{SC}).[1,4,24] In such a cell, other properties become Se-dependent besides mobilities: bandgap, electron affinity, and the corresponding conduction band offset (CBO) at the front interface, absorption coefficient, carrier lifetimes, and acceptor ionization levels.

To simulate the effect of Se grading on solar cell performance, we implement a drift-diffusion model with spatially dependent absorber properties defined by the Se profile. We use a linear Se grading model, where the Se concentration changes from the "peak Se" value at the front interface to 0% at the back interface (**Figure** 5a). The peak Se value varies from 0% to 30%. We define the values of parameters for 0% and 30% Se concentrations (**Table** 2), and the values for all intermediate concentrations are defined by linear interpolation. We use a compensated doping model with an acceptor density of 1.01×10^{18} cm^{-3} and a donor density of 10^{18} cm^{-3} so that the net doping corresponds to the CV-measured value of 10^{16} cm^{-3} for As-doped devices. With the compensated doping model, when the acceptor ionization level is non-shallow, the free hole density is lower than the net doping defined by the difference between acceptors and donors.[51] Additionally, we set up 10^5 cm^{-2} of deep acceptors at the front interface and a valence band offset of −0.15 eV and a deep donor density of 10^7 cm^{-2} at the back interface.

Simulation results suggest that with a graded Se profile, low hole mobility has a detrimental effect on device performance (Figure 5b–d). No J_{SC} loss is observed for any peak Se concentration analyzed, even with the lowest hole mobility of 0.5 cm^2 Vs^{-1} in the high-Se region. A minor V_{OC} loss of up to 10 mV is predicted by the model with a 30% peak Se concentration. The main

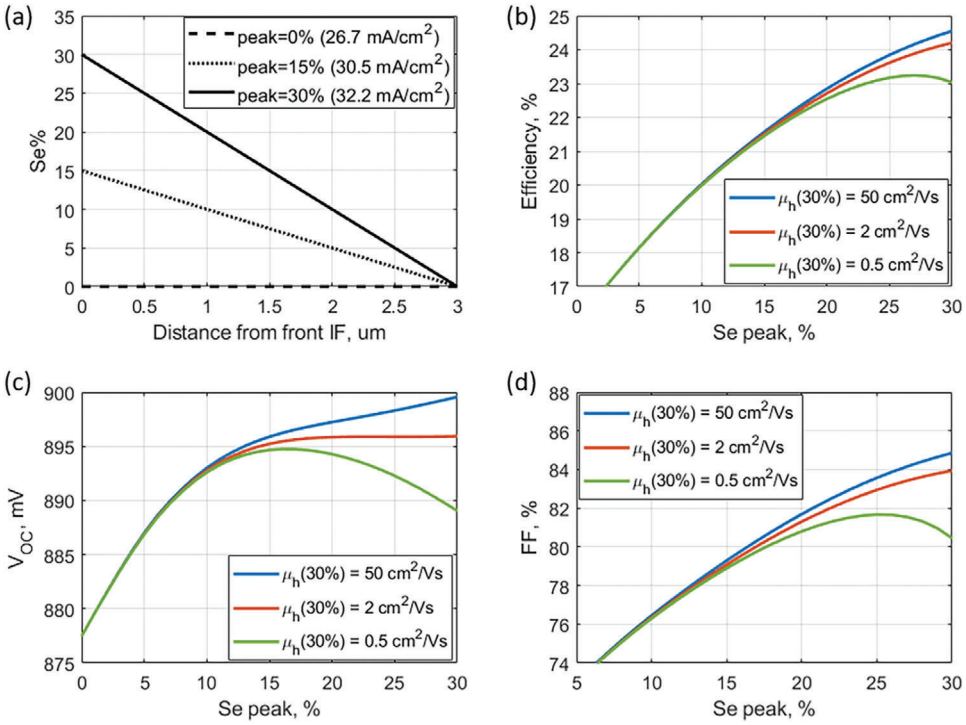

Figure 5. a) Linear Se% grading model for 3 peak Se concentrations (0%, 15%, 30%). b–d) Simulated dependence of efficiency, V_{OC}, and FF on peak Se for three different values of hole mobility in 30% Se.

factor limiting performance growth with increasing peak Se concentration is fill factor (FF) loss. The model predicts FF increases with increasing peak Se concentration due to increased lifetime, reduced CBO, and electron affinity grading. However, at high peak Se concentrations, FF becomes sensitive to hole mobility. Up to 5% FF loss is observed in this model when hole mobility reduces from 50 to 0.5 cm^2 Vs^{-1} in 30% Se. As a result, even though J_{SC} and FF grow with peak Se concentration, efficiency eventually saturates, which prevents efficiencies from reaching 24–25%.

Simulated performance metrics for peak Se of 25–30% and $\mu_h(30\%) = 0.5–2$ cm^2 Vs^{-1} roughly correspond to the measured performance metrics of the latest CdSeTe record cell.[4] Other models may also be able to simulate real device performance, and a thorough model fit to additional experimental data is required to conclude on model uniqueness. However, it is reasonable that our model qualitatively reflects the main trends and losses in real devices. In this case, low hole mobility in the high-Se region may represent a real limitation for further FF improvement, especially for high-J_{SC} devices with high Se concentrations.

Another hole-mobility-dependent effect suggested by device modeling is the possibility of inflated quasi-Fermi-level splitting in the front region of the absorber when the partial hole conductivity is very low. When the partial conductivity, which is the product of mobility and hole density, is low, the hole quasi-Fermi level does not fully "equilibrate" between the high-generation region near the front and the rest of the absorber. This results in nonuniform quasi-Fermi-level splitting with higher splitting near the front. As a result, optical metrics such as external radiative efficiency and implied voltage (quasi-Fermi level splitting) may not accurately represent the "absorber quality." This effect is amplified by compensated p-doping, where the net doping is considerably less than the total acceptor density, and by nonshallow acceptor ionization levels, which is the case for CdSeTe absorber. More details will be published elsewhere.[52]

4. Conclusions and Outlook

CdTe is the only thin film technology to demonstrate large-scale manufacturability and long-term reliability.[24] It is cost-competitive with crystalline PV and has lower embedded energy and carbon.[53] To further reduce cost per watts, efficiency improvements are needed. Loss analysis and defect models guide and benchmark such improvements.

We show that electronic defects in high-efficiency As-doped CdSeTe solar cells[1,4,24] are more complex than usually assumed

Table 2. Se-dependent properties in the device model.

Se concentration	Hole mobility, cm^2 Vs^{-1}	Lifetime, ns	Eg (300 K), eV	CBO, eV	Acceptor ionization level, eV
0%	50	400	1.5	−0.40	0.13
30%	50, 2, 0.5	4	1.39	−0.20	0.16

in solar cell models,[16,17,18,27,28] and more complex than defects in perovskites[15,54] or Cu(In,Ga)Se_2.[29,55] Our work builds on recent observations of sub-bandgap emission in CdSeTe,[10–14] develops a more detailed understanding of charge carrier transport and recombination, and examines the impact on state-of-the-art solar cells. We showed that electronic defects at Se-sites are present at low and high As incorporation and they reduce charge carrier diffusion length to less than the typical absorber thickness (L_{diff} <1.5 µm) even when charge carrier lifetimes approach the radiative limit. We used device simulations to show that absorber bandgap grading while increasing the current, does not alleviate fill factor losses due to reduced diffusion length. Estimated maximal efficiency (≈23%) is similar to the current efficiency record.[3,4] Electronic defects identified here appear to be similar to the long-recognized anion-site disorder in II–VI semiconductors.[25,37,38] Similar transition to disordered transport was observed for some perovskites[56] and kesterites.[57] Unlike these cases where disorder led to reduced performance, the highest-performing CdSeTe solar cell devices have a large density of sub-bandgap defect states. In this aspect, CdTe PV appears to be distinctly different from other state-of-the-art PV technologies.

What is the possible path forward toward 25% and higher efficiency? In addition to doping and lifetime,[7] front[58,59] and back[60,61] contact details, an electronic disorder in the absorber needs to be considered and reduced. Earlier studies analyzed bandgap fluctuations,[62] Urbach band tails,[63] and electrostatic potential fluctuations.[40] In these cases, authors investigated radiative voltage, not transport, and applied thermodynamic solar cell models. Based on our results, it appears that more detailed solar cell models are needed for CdSeTe.

For 25% efficient CdSeTe solar cells, it appears that anion site defects, primarily due to Se, need to be better controlled. Absorber selenization and grading enabled industry-leading Cu(In,Ga)Se_2 and (Ag,Cu)(In,Ga)Se_2 solar cells.[64] That work was aimed at reducing V_{Se}–V_{Cu} divacancy density, as such divacancies result in metastability[65] and band tails[66] in Cu(In,Ga)Se_2. Perhaps a similar control of Se composition applied to reduce anion vacancy density will enable CdSeTe solar cell advances. Radiative emission spectra identify near-E_g defects in Cu(In,Ga)Se_2[64,66,67] and CdSeTe,[10–14] providing inputs to device models and enabling defect metrology.

5. Experimental Section

Fabrication and Characterization of Heterostructures and Solar Cells: Heterostructures with uniform and graded bandgap were fabricated by vapor transport deposition (VTD) with and without in situ As doping, as described by First Solar.[1,4] Samples used for spectroscopy did not have back contacts. Sister samples used to measure net doping using capacitance-voltage (CV) had ZnTe back contacts. As incorporation was measured by SIMS (secondary ion mass spectrometry). Bulk As concentrations were 3×10^{17} cm^{-3} (As background) and (1–3) $\times$ 10^{18} cm^{-3} (As doped).

Spectroscopy: Absolute PL emission spectra were measured with 632.8 nm cw (constant wave) excitation using Si and InGaAs detectors (Pixis F100 Si CCD and PyLoNIR 1024 InGaAs linear array, Princeton Instruments). The spectral response was corrected using calibration sources provided by the manufacturer, and absolute photon numbers were obtained using reflectance standards (Lab Sphere).[10] TRPL was measured using excitation at 640 nm (300 fs pulses) and time-correlated single photon counting (Picoharp 300, Picoquant). Avalanche photodiode (APD, Micro Photon Devices) was used for photon counting, emission wavelength was selected using bandpass filters.[68]

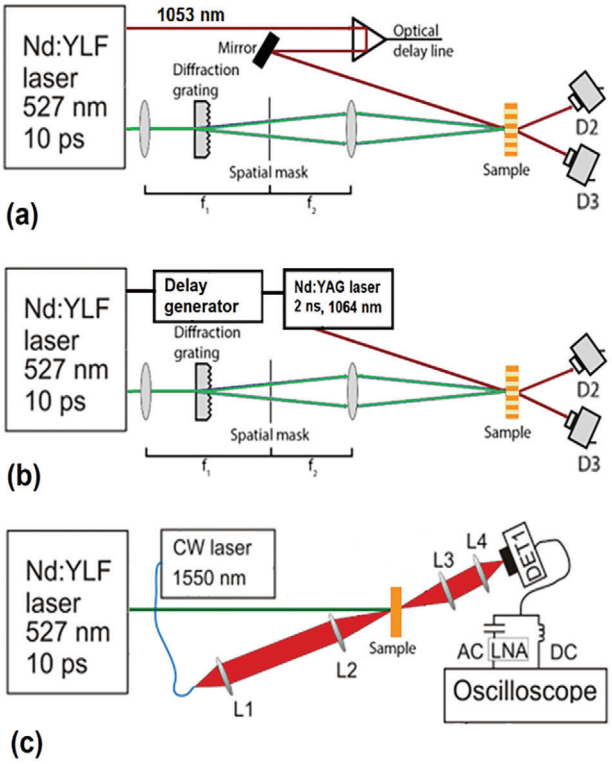

Scheme 2. Illustration of LITG and PP measurement setups.

For ps-resolution LITG (**Scheme 2a**), Nd:YLF laser was used (PL2243, EKSPLA, 10 ps pulses at 10 Hz). Excitation (527 nm, 2nd harmonics) was split by a diffraction grating creating carrier-density modulated LITG. By using the optical delay line (Aerotech ACT115DL) diffraction efficiency (described by the ratio of detector D2 and D3 readings) kinetics were obtained using 10 ps 1053 nm probe pulses. For ns-resolution LITG (Scheme 2b) excitation was the same and probing was with the synchronized pulsed Nd:YAG laser (NL202, EKSPLA, 2 ns pulses at 1064 nm). The delay was controlled by a digital generator (Highland Technology P400).[56]

The same Nd:YLF laser was used for excitation in PP measurements (Scheme 2c). A single-mode 1550 nm cw laser (Eblana Photonics) was used for probing. Transmitted probe intensity was monitored with 5 GHz bandwidth biased InGaAs photodetector DET1 (Thorlabs DET08CFC/M), 10 kHz-2 GHz bandwidth low noise amplifier (LNA), and 6 GHz LeCroy oscilloscope (SDA 6000). Decay kinetics were averaged 100 times with and without excitation, measurement resolution was ≈0.5 ns.[69]

Device Modeling: The solar cell model consists of 0.5 µm n-TCO, 3 µm CdSeTe absorber, and 0.1 µm p-ZnTe. Negative CB/VB band offsets at front/back interfaces correspond to reduced front[70] and back[71] interface bandgaps in comparison CdSeTe. The numerical model solves drift-diffusion and reaction equations for electrons and holes and the Poisson equation for charge conservation. Equations are discretized using the finite volume method (in 1D) with 400 mesh points and solved simultaneously using a custom-damped Newton method with an analytical Jacobian. Solutions are verified against the SCAPS 1D solar simulator.[72] More details on our numerical solver will be published elsewhere.[73]

Supporting Information

Supporting Information is available from the Wiley Online Library or from the author.

Acknowledgements

This work was authored in part by the National Renewable Energy Laboratory, operated by Alliance for Sustainable Energy, LLC, for the U.S. Department of Energy (DOE) under Contract No. DE-AC36-08GO28308. The views expressed in the article do not necessarily represent the views of the DOE or the U.S. Government. The U.S. Government retains and the publisher, by accepting the article for publication, acknowledges that the U.S. Government retains a nonexclusive, paid-up, irrevocable, worldwide license to publish or reproduce the published form of this work, or allow others to do so, for U.S. Government purposes. At NREL and BGSU, this material is based upon work supported by the U.S. Department of Energy's Office of Energy Efficiency and Renewable Energy (EERE) under the Solar Energy Technology Office (SETO) Award Number 38 525. P.Š. acknowledges the "Universities' Excellence Initiative" programme by the Ministry of Education, Science and Sports of the Republic of Lithuania under the agreement with the Research Council of Lithuania (project No. S-A-UEI-23-6).

Conflict of Interest

The authors declare no conflict of interest.

Data Availability Statement

The data that support the findings of this study are available from the corresponding author upon reasonable request.

Keywords

CdTe, characterization, loss analysis, thin film solar cells

Received: August 28, 2024
Revised: October 1, 2024
Published online:

[1] W. K. Metzger, S. Grover, D. Lu, E. Colegrove, J. Moseley, C. L. Perkins, X. Li, R. Mallick, W. Zhang, R. Malik, J. Kephart, C.-S. Jiang, D. Kuciauskas, D. S. Albin, M. M. Al-Jassim, G. Xiong, M. Gloeckler, *Nat Energy* **2019**, *4*, 837.
[2] https://investor.firstsolar.com/news/news-details/2024/First-Solar-Commissions-Western-Hemispheres-Largest-Solar-RD-Center/default.aspx (accessed: August 2024).
[3] https://www.nrel.gov/pv/cell-efficiency.html (accessed: August 2024).
[4] R. Mallick, X. Li, C. Reich, X. Shan, W. Zhang, T. Nagle, L. Bok, E. Bicakci, N. Rosenblatt, D. Modi, R. Farshchi, C. Lee, J. Hack, S. Grover, N. Wolf, W. K. Metzger, D. Lu, G. Xiong, *IEEE J. Photovoltaics* **2023**, *13*, 510.
[5] S. Rühle, *Solar Energy* **2016**, *130*, 139.
[6] https://www.nrel.gov/pv/module-efficiency.html (accessed: August 2024).
[7] A. Kanevce, M. O. Reese, T. M. Barnes, S. A. Jensen, W. K. Metzger, *J. Appl. Phys.* **2017**, *121*, 214506.
[8] M. Amarasinghe, D. Albin, D. Kuciauskas, J. Moseley, C. L. Perkins, W. K. Metzger, *Appl. Phys. Lett.* **2021**, *118*, 211102.
[9] D. Kuciauskas, J. M. Kephart, J. Moseley, W. K. Metzger, W. S. Sampath, P. Dippo, *Appl. Phys. Lett.* **2018**, *112*, 263901.
[10] D. Kuciauskas, M. Nardone, A. Bothwell, D. Albin, C. Reich, C. Lee, E. Colegrove, *Adv. Energy Mater.* **2023**, *13*, 2301784.
[11] G. Hu, H. Cao, P. Tang, X. Hao, B.-H. Li, H. Li, D. Zhao, W. Li, L. Wu, J. Zhang, *Solar Energy* **2023**, *258*, 289.
[12] G. R. Neupane, A. J. Winchester, N. M. Peraca, D. S. Albin, J. N. Duenow, M. O. Reese, S. J. Pookpanratana, S. M. Thon, B. H. Hamadani, *Cell Rep. Phys. Sci.* **2023**, *4*, 101522.
[13] B. Frouin, T. Bidaud, S. Pirotta, T. Ablekim, J. Moseley, W. K. Metzger, S. Collin, *APL Mater.* **2024**, *12*, 031135.
[14] D. L. McGott, S. W. Johnston, C. Jiang, T. Liu, D. Kuciauskas, S. Glynn, M. O. Reese, *Adv. Sci.* **2024**, *11*, 2309264.
[15] T. Kirchartz, J. A. Márquez, M. Stolterfoht, T. Unold, *Adv. Energy Mater.* **2020**, *10*, 1904134.
[16] M. A. Green, A. W. Y. Ho-Baillie, *ACS Energy Lett.* **2019**, *4*, 1639.
[17] T. Kirchartz, U. Rau, *Adv. Energy Mater.* **2018**, *8*, 1703385.
[18] S. Akel, A. Kulkarni, U. Rau, T. Kirchartz, *PRX Energy* **2023**, *2*, 013004.
[19] B. Fluegel, K. Alberi, M. J. DiNezza, S. Liu, Y.-H. Zhang, A. Mascarenhas, *Phys. Rev. Appl.* **2014**, *2*, 034010.
[20] D. Kuciauskas, S. Farrell, P. Dippo, J. Moseley, H. Moutinho, J. V. Li, A. M. Motz, A. Kanevce, K. Zaunbrecher, T. A. Gessert, D. H. Levi, W. K. Metzger, E. Colegrove, S. Sivananthan, *J. Appl. Phys.* **2014**, *116*, 123108.
[21] D. Kuciauskas, J. Moseley, P. Ščajev, D. Albin, *Phys. Status Solidi RRL* **2020**, *14*, 1900606.
[22] P. Ščajev, A. Mekys, L. Subačius, S. Stanionytė, D. Kuciauskas, K. G. Lynn, S. K. Swain, *Sci. Rep.* **2022**, *12*, 12851.
[23] C. Reich, *Investigations to Improve CdTe Based Solar Cell Open Circuit Voltage and Efficiency Using Passivation and Selectivity Theoretical Framework*, Colorado State University, Fort Collins, CO **2022**.
[24] M. A. Scarpulla, B. McCandless, A. B. Phillips, Y. Yan, M. J. Heben, C. Wolden, G. Xiong, W. K. Metzger, D. Mao, D. Krasikov, I. Sankin, S. Grover, A. Munshi, W. Sampath, J. R. Sites, A. Bothwell, D. Albin, M. O. Reese, A. Romeo, M. Nardone, R. Klie, J. M. Walls, T. Fiducia, A. Abbas, S. M. Hayes, *Sol. Energy Mater. Sol. Cells* **2023**, *255*, 112289.
[25] D. Lee, A. Mysyrowicz, A. V. Nurmikko, B. J. Fitzpatrick, *Phys. Rev. Lett.* **1987**, *58*, 1475.
[26] A. Onno, C. Reich, S. Li, A. Danielson, W. Weigand, A. Bothwell, S. Grover, J. Bailey, G. Xiong, D. Kuciauskas, W. Sampath, Z. C. Holman, *Nat. Energy* **2022**, *7*, 400.
[27] M. H. Wolter, R. Carron, E. Avancini, B. Bissig, T. P. Weiss, S. Nishiwaki, T. Feurer, S. Buecheler, P. Jackson, W. Witte, S. Siebentritt, *Prog. Photovolt.* **2022**, *30*, 702.
[28] J. Wong, S. T. Omelchenko, H. A. Atwater, *ACS Energy Lett.* **2021**, *6*, 52.
[29] D. Abou-Ras, *J. Vac. Sci. Technol. A* **2024**, *42*, 022803.
[30] J. Moseley, D. Krasikov, C. Lee, D. Kuciauskas, *J. Appl. Phys.* **2021**, *130*, 163105.
[31] D. Kuciauskas, C. L. Perkins, M. Nardone, C. Lee, R. Mallick, G. Xiong, *Solar RRL* **2023**, *7*, 2300073.
[32] J. Yang, S.-H. Wei, *Chinese Phys. B* **2019**, *28*, 086106.
[33] W. Stadler, D. M. Hofmann, H. C. Alt, T. Muschik, B. K. Meyer, E. Weigel, G. Müller-Vogt, M. Salk, E. Rupp, K. W. Benz, *Phys. Rev. B* **1995**, *51*, 10619.
[34] T. Markvart, in *Recombination in Semiconductors*, 1st ed., Cambridge University Press, England **1992**, pp. 447–480.
[35] M. J. S. Brasil, P. Motisuke, F. Decker, J. R. Moro, *J. Phys. C: Solid State Phys.* **1988**, *21*, 3141.
[36] S.-H. Wei, S. B. Zhang, *J. Phys. Chem. Solids* **2005**, *66*, 1994.
[37] S. Permogorov, A. Reznitsky, *J. Lumin.* **1992**, *52*, 201.
[38] C. Gourdon, P. Lavallard, *J. Cryst. Growth* **1990**, *101*, 767.
[39] J. Xue, X. Yang, X. Bao, L. Fu, S. Li, M. Huang, J. Wang, H. Song, S. Chen, C. Chen, K. Li, J. Tang, *ACS Appl. Mater. Interfaces* **2023**, *15*, 17858.
[40] J. Moseley, S. Grover, D. Lu, G. Xiong, H. L. Guthrey, M. M. Al-Jassim, W. K. Metzger, *J. Appl. Phys.* **2020**, *128*, 103105.

[41] W. K. Metzger, D. Albin, D. Levi, P. Sheldon, X. Li, B. M. Keyes, R. K. Ahrenkiel, *J. Appl. Phys.* **2003**, *94*, 3549.
[42] L. Krückemeier, B. Krogmeier, Z. Liu, U. Rau, T. Kirchartz, *Adv. Energy Mater.* **2021**, *11*, 2003489.
[43] P. Ščajev, S. Miasojedovas, A. Mekys, D. Kuciauskas, K. G. Lynn, S. K. Swain, K. Jarašiūnas, *J. Appl. Phys.* **2018**, *123*, 025704.
[44] N. F. Mott, E. A. Davis, *Electronic Processes in Non-Crystalline Materials*, Oxford University Press, Oxford **2012**.
[45] M. Nardone, M. Spehar, D. Kuciauskas, D. S. Albin, *J. Appl. Phys.* **2020**, *127*, 223104.
[46] D. Kuciauskas, P. Dippo, Z. Zhao, L. Cheng, A. Kanevce, W. K. Metzger, M. Gloeckler, *IEEE J. Photovoltaics* **2016**, *6*, 313.
[47] D. Kuciauskas, P. Dippo, A. Kanevce, Z. Zhao, L. Cheng, A. Los, M. Gloeckler, W. K. Metzger, *Appl. Phys. Lett.* **2015**, *107*, 243906.
[48] A. Abudulimu, S. Carter, A. B. Phillips, D. Li, S. Neupane, T. Brau, J. Friedl, E. Bastola, M. K. Jamarkattel, M. J. Heben, Y. Yan, R. J. Ellingson, *Solar RRL* **2024**, *8*, 2400131.
[49] D. Kuciauskas, J. Moseley, C. Lee, *Sol. RRL* **2021**, *5*, 2000775.
[50] C. H. Swartz, M. Edirisooriya, E. G. LeBlanc, O. C. Noriega, P. A. R. D. Jayathilaka, O. S. Ogedengbe, B. L. Hancock, M. Holtz, T. H. Myers, K. N. Zaunbrecher, *Appl. Phys. Lett.* **2014**, *105*, 222107.
[51] K. K. Chin, *Sol. Energy Mater. Sol. Cells* **2010**, *94*, 1627.
[52] D. Krasikov, D. Kuciauskas, P. Ščajev, R. Farshchi, K. McReynolds, I. Sankin, Understanding ERE and iVOC metrics for graded CdSeTe absorbers, submitted, https://doi.org/10.22541/au.172647331.12093833/v1.
[53] H. M. Wikoff, S. B. Reese, M. O. Reese, *Joule* **2022**, *6*, 1710.
[54] G. J. W. Aalbers, T. P. A. Van Der Pol, K. Datta, W. H. M. Remmerswaal, M. M. Wienk, R. A. J. Janssen, *Nat. Commun.* **2024**, *15*, 1276.
[55] O. Ramírez, J. Nishinaga, F. Dingwell, T. Wang, A. Prot, M. H. Wolter, V. Ranjan, S. Siebentritt, *Solar RRL* **2023**, *7*, 2300054.
[56] P. Ščajev, R. Aleksiejunas, S. Miasojedovas, S. Nargelas, M. Inoue, C. Qin, T. Matsushima, C. Adachi, S. Juršėnas, *J. Phys. Chem. C* **2017**, *121*, 21600.
[57] C. J. Hages, A. Redinger, S. Levcenko, H. Hempel, M. J. Koeper, R. Agrawal, D. Greiner, C. A. Kaufmann, T. Unold, *Adv. Energy Mater.* **2017**, *7*, 1700167.
[58] T. Song, A. Kanevce, J. R. Sites, *J. Appl. Phys.* **2016**, *119*, 233104.
[59] T. Ablekim, E. Colegrove, W. K. Metzger, *ACS Appl. Energy Mater.* **2018**, *1*, 5135.
[60] G. K. Liyanage, A. B. Phillips, M. J. Heben, *APL Mater.* **2018**, *6*, 101104.
[61] G. K. Liyanage, A. B. Phillips, F. K. Alfadhili, R. J. Ellingson, M. J. Heben, *ACS Appl. Energy Mater.* **2019**, *2*, 5419.
[62] U. Rau, J. H. Werner, *Appl. Phys. Lett.* **2004**, *84*, 3735.
[63] J. Jean, T. S. Mahony, D. Bozyigit, M. Sponseller, J. Holovský, M. G. Bawendi, V. Bulović, *ACS Energy Lett.* **2017**, *2*, 2616.
[64] A. M. Bothwell, S. Li, R. Farshchi, M. F. Miller, J. Wands, C. L. Perkins, A. Rockett, A. R. Arehart, D. Kuciauskas, *Solar RRL* **2022**, *6*, 2200230.
[65] S. Lany, A. Zunger, *J. Appl. Phys.* **2006**, *15*, 100113725.
[66] S. A. Jensen, A. Kanevce, L. M. Mansfield, S. Glynn, S. Lany, D. Kuciauskas, *Sci. Rep.* **2017**, *7*, 13788.
[67] A. J. Ferguson, R. Farshchi, P. K. Paul, P. Dippo, J. Bailey, D. Poplavskyy, A. Khanam, F. Tuomisto, A. R. Arehart, D. Kuciauskas, *J. Appl. Phys.* **2020**, *127*, 215702.
[68] D. Kuciauskas, *Advanced Characterization of Thin Film Solar Cells*, (Eds. M. Al-Jassim, N. Haegel), The Institution of Engineering and Technology, London, U.K **2020**, p. 191.
[69] P. Ščajev, V. Soriūtė, G. Kreiza, S. Nargelas, D. Dobrovolskas, T. Malinauskas, L. Subačius, P. Onufrijevs, S. Varnagiris, H.-H. Cheng, *Mater. Sci Eng. B* **2021**, *270*, 115204.
[70] A. Sharan, M. Nardone, D. Krasikov, N. Singh, S. Lany, *Appl. Phys. Rev.* **2022**, *9*, 041411.
[71] P. Gorai, D. Krasikov, S. Grover, G. Xiong, W. K. Metzger, V. Stevanović, *Sci. Adv.* **2023**, *9*, eade3761.
[72] M. Burgelman, P. Nollet, S. Degrave, *Thin Solid Films* **2000**, *361–362*, 527.
[73] K. McReynolds, D. Krasikov, I. Sankin, E-Solver: flexible, robust, and performant 1D device solver for thin-film photovoltaics, in preparation.